

Method of Analysis of Saturation Collapse Behavior

Yuji KOHGO

*Crop Production and Postharvest Technology Division,
Japan International Research Center for Agricultural Sciences (JIRCAS)
(Tsukuba, Ibaraki, 305 Japan)*

Received May 2, 1996

Abstract

We present a consolidation analysis method coupled with an elastoplastic constitutive model for unsaturated soils. The elastoplastic model includes two suction effects related to the increase in effective stresses, yield stress and resistance to plastic deformation due to the increase in suction. The smooth transition from elasticity to plasticity was also achieved by introducing the subloading surface model. The consolidation analysis method employs force equilibrium equations for soil and the Richards' mass conservation equation of pore water as field equations and is formulated by using FEM. Three simulations of typical element test series, a seepage model test and a virtual earth dam during reservoir filling were performed using the consolidation analysis method. The simulation results showed that the consolidation analysis method could be used to analyze geomechanical static problems relating to pore water pressure changes, especially saturation collapse behavior.

Additional key words : effective stress, consolidation analysis, constitutive equation of soil, plasticity, unsaturated soil

Notations

D_{ijkl}	elastic modulus tensor	I_c	yield stress
E_f	$= \partial S_r / \partial s$,	\bar{I}_c	value of I_c on subloading surfaces
E'_f	$= E_f / n$	I_1	first stress invariant
F_i	components of body force vector	J_2	second invariant of deviator stress
G	shear modulus	J_3	third invariant of deviator stress
G_i	material parameter for shear modulus	K	bulk modulus
H	hardening modulus	K_i	material parameter for bulk modulus
\hat{H}	hardening modulus at conjugate point	L	loading function

P_a	atmospheric pressure	α	coefficient characterizing single-step temporal discretization
R	material parameter which defines the aspect ratio of elliptical yield surface	α_h	material parameter for hardening modulus
\overline{R}	ratio of sizes of the subloading surfaces to the normal yield surfaces	γ	unit weight of soil
\overline{R}_i	initial value of \overline{R} along a loading process	γ_j	material parameter for shear modulus
S_r	degree of saturation	γ_p	material parameter for shear modulus
S_{re}	degree of saturation at air entry	ε_{ii}	volumetric strain of soil skeleton
a_e	material parameter for effective stress	ε_v^p	plastic volumetric strain
a_{ii}	change of storage of water due to change of degree of saturation	$\dot{\varepsilon}_{ij}$	strain increment tensor
a_s	material parameter for state surface	$\dot{\varepsilon}_{ij}^p$	plastic strain increment tensor
c	$1/E_f$, tangential slope of soil water retention curve	θ	Lode angle
e_0	initial void ratio	κ	slope of $e - \log p'$ curve at unloading
e_0^0	material parameter for state surface	λ	value of λ^* at saturation
f	yield functions	λ^*	slope of $e - \log p'$ curves in plastic range
h	arbitrary constant which satisfies $h \gg H$	λ^*_0	initial value of λ^*
h_s	Henry's coefficient of solubility	σ	total stress
k_s	permeability at saturation	σ'	effective stress
m_p	material parameter for permeability	σ'_{ij}	current effective stress tensor
m_r	parameter for soil water retention curve	$\hat{\sigma}'_{ij}$	effective stress tensor at conjugate point
n	porosity	$\dot{\sigma}'_{ij}$	effective stress increment
n_{ij}	unit tensor of plastic loading at the conjugate point	ϕ'	internal friction angle of failure line
\overline{n}_{ij}	unit gradient tensor of plastic potential at conjugate point	ϕ'_{cs}	internal friction angle of critical state line
n_p	material parameter for permeability	Ψ	plastic potential functions
n_r	parameter for soil water retention curve	\mathbf{B}	nodal displacement - strain matrix
n_s	material parameter for state surface	\mathbf{C}	nodal displacement - volumetric strain matrix
p'	effective mean stress	\mathbf{D}	elasticity matrix
p'_0	initial mean effective stress	\mathbf{F}	body force vector
q_i	components of relative displacement velocity vector of water with respect to soil skeleton	\mathbf{K}^*_0	coefficient matrix
s	suction	\mathbf{N}	interpolation function for pore water pressure
s^*	effective suction	\mathbf{N}'	gradient matrix for pore water pressure
s_c	critical suction	\mathbf{N}_u	interpolation function for displacement
s_e	air entry suction	\mathbf{Q}_b	prescribed flux on boundary nodal points
u_a	pore air pressure	\mathbf{R}	permeability matrix
u_{eq}	equivalent pore pressure	\mathbf{T}_b	prescribed traction on boundary nodal points
u_w	pore water pressure	\mathbf{a}	change of storage of water due to change of degree of saturation
Γ	value of Γ^* at saturation	\mathbf{q}	flux vector
Γ^*	void ratio of a constant $e - \log p'$ curve in plastic range with $p' = \text{unit}$	\mathbf{u}	nodal displacement vector
Γ^*_0	initial value of Γ^*	u_w	nodal pore water pressure
		Φ	residual vector
		δ	unknown vector
		σ'	effective stress vector

Introduction

The compressive deformation of soils with saturation is called "Saturation collapse" or "Collapse due to wetting". The saturation collapse refers to the rearrangement of particles and a great loss of volume upon wetting. As the amount of deformation due to wetting is large, the saturation collapse causes serious damage to the structures constructed on or with the soils. Figure 1 shows an example of saturation collapse behavior in a laboratory test⁴⁾. The vertical stress is plotted against the void ratio e . The soil is considerably stiff within unsaturated ranges AB or A'B' as shown in Fig.1. However, once the soil is soaked under the application of a constant load, a large amount of compressive deformation, namely saturation collapse occurs (see the change B' → C'). The deformation is irrecoverable. The stress point C' after soaking lies on the loading line (CD line) obtained under saturated conditions. This is the typical saturation collapse behavior. The collapse behavior can also be seen in soils compacted on

the dry side of optimum water content. For the construction of irrigation facilities using soil materials, for example fill-type dams, it is therefore very important to investigate the possibility of saturation collapse of the soils.

The saturation collapse behavior is one of the typical properties of unsaturated soils and has been one of the most difficult problems to estimate in the field of soil mechanics for a long time. A few groups of researcher^{1, 7, 8)} have attempted to address the problem on the basis of the elastoplastic theory since the end of the 1980s. We have developed elastoplastic models which may estimate the saturation collapse^{10, 11, 12, 13)}

We need to use the stress-seepage coupled analysis methods^{9, 13, 15, 18)}, so called the consolidation analysis methods in order to estimate the real problems associated with the saturation collapse. Here, we describe the consolidation analysis method coupled with the elastoplastic model for unsaturated soils. The verification of the method is examined through three simulations of typical element test series, a seepage model test and the behavior of a virtual earth dam during reservoir filling.

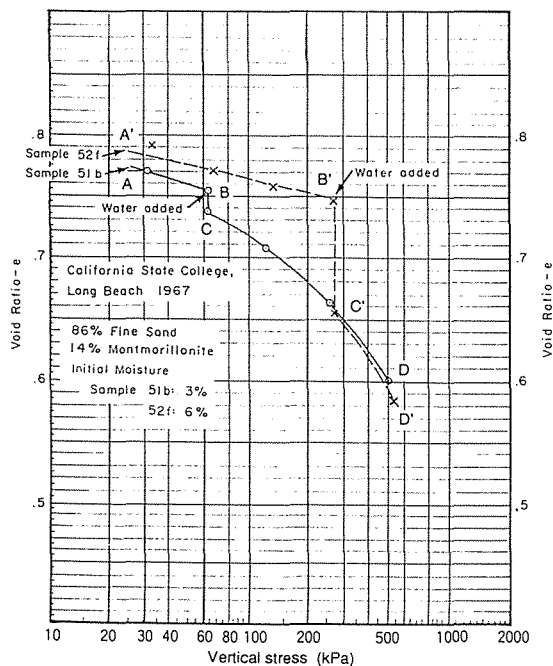


Fig. 1. Typical saturation collapse (after Dudley (1970)⁴⁾)

Generalized Elastoplastic Model for Unsaturated Soils

The stress - strain relationship of unsaturated soils is greatly influenced by the amount of matric suction and the retention conditions of pore water. First, we examine the suction effects on each saturation condition. Then we show how the suction effects are introduced into an elastoplastic model. The elastoplastic model proposed here is the first one for unsaturated soils that belongs to the category of cyclic plasticity⁶⁾. The normal yield surfaces and subsurfaces therefore have to be defined.

1) Suction effects

Matric suction may only be referred to as suction, hereafter. Suction s is defined as

$$s = u_a - u_w \tag{1}$$

where u_a is the pore air pressure and u_w the pore water pressure.

It is also necessary to define the effective suction s^* , since suction effects are assumed to be the functions of s^* . The effective suction is

$$s^* = \langle s - s_e \rangle \tag{2}$$

where s_e is the air entry suction and the brackets $\langle \rangle$ denote the operation $\langle z \rangle = z$ at $z > 0$ and $\langle z \rangle = 0$ at $z \leq 0$.

According to Ref. 11, the possible saturation conditions (or retention conditions) may be divided into three groups; Insular air, Fuzzy and Pendular saturation conditions as shown in Table 1. When $s \leq s_e$ the saturation condition is called insular air saturation where pore air only exists as air bubbles surrounded by water. In insular air saturation, the mechanical soil behavior can be explained in terms of effective stresses that can be estimated by

Terzaghi's effective stress equation used for completely saturated soils.

$$\sigma' = \sigma - u_w \tag{3}$$

Where σ' is the effective stress and σ the total stress.

When the value of suction s is very high, water may only be present in the menisci formed around the grain contact points. This saturation condition is called pendular saturation. In pendular saturation, the attractive force, known as capillary force, is induced by the surface tension between pore air and pore water and it draws the soil particles together. The capillary force increases as suction increases. An increase in the capillary force inhibits the plastic deformation associated with the relative sliding between the particles due to the external force. An increase in suction therefore induces the suction effect (b); capillary force due to an increase in suction induces an increase in yield stress and resistance to the plastic

Table 1. The possible saturation conditions and their suction effects

Saturation conditions	Conditions of pore water and air	Suction effects	Region of each saturation condition
Insular air saturation	Pore air may only exist as air bubbles surrounded by water.	(a) Increase in suction only increases effective stresses which can be estimated using Terzaghi's equation.	
Fuzzy saturation	In small pores, the condition is the insular air saturation, while it is the pendular saturation in large pores.	(a) Increase in effective stresses due to an increase in suction, can be estimated using Eqs. (4)-(6) which are newly defined. (b) Increase in yield stress and resistance to the plastic deformation due to suction, can be estimated using Eqs.	
Pendular saturation	Pore water may only exist in menisci formed around grain contact points.	(b) Capillary force due to increase in suction induces an increase in yield stress and resistance to plastic deformation.	

deformation. This suction effect will be described in detail in the discussion of fuzzy saturation.

If the value of suction s is greater than that of the air entry suction s_e , air will enter the soil pores. As real soil has pores with various sizes, a large amount of water in large pores is drained and a small amount of water may remain in the meniscuses formed around grain contact points, while the small pores are saturated until higher suction is attained. This saturation condition is called fuzzy saturation. In fuzzy saturation, the mechanical behavior is affected by the following 4 points.

- (1) Effective stress increases with an increase in suction in saturated zone.
- (2) The saturation zone decreases with an increase in suction.
- (3) Capillary force increases with an increase in suction in unsaturated zone.
- (4) Internal confinement, that is, the inhibition of overall deformations of the soil caused by the Point (3) becomes greater as suction increases.

Before we start the main discussion, we have to define what the uniform behavior of soil is and under which conditions it exists. The uniform behavior refers to the behavior where no internal confinement can be found. For example, as slippage between soil particles occurs anywhere in soil on the critical state line at the wet side of critical state, the behavior is uniform. The wet and dry sides of critical state respectively mean the normally consolidation and overconsolidation sides of critical state. The definition is the same as that in the Critical State Soil Mechanics²⁾.

The phenomenon of the Point (4) induces dilatancy, which is similar to that induced by interlocking, and makes the soil behavior non-uniform. The Point (4) is the overall confinement of soil induced by the Point (3) and cannot be estimated until the elastoplastic theory is introduced. It is namely treated as an expansion of yield surface (an increase in yield stress) due to increasing suction which is the same manner as that employed in the case of consideration of

interlocking effects due to application of preconsolidation pressure. If the capillary force is rather smaller than the applied external forces, the uniform soil behavior may occur. If the soil behavior due to the applied external forces is uniform, the behavior may be expressed using stresses defined in the continuum mechanics. Comparing shear strength between saturated and unsaturated soils in the uniform shear behavior, we may consider that *the extra-confining stresses* apply to the unsaturated soil¹¹⁾. These extra-confining stresses are *the effective confining stresses* and may be considered to be *the effective stresses*. The effective stresses can namely be defined as follows. *When the effects concerned with the Points (1) ~ (3) can be regarded as the effect of an increase in effective confined stresses, the effective confined stresses will be defined as effective stresses.*

Here, effective stress equations are assumed to be formulated using the relationship between the shear strength and suction on the wet side of the critical state. According to the experimental results¹⁶⁾ (see Fig. 2), it is reasonable to define the following empirical effective stress equations (Suction effect (a)).

$$\sigma' = \sigma - u_{eq} \tag{4}$$

$$u_{eq} = u_a - s \quad (s \leq s_e) \tag{5}$$

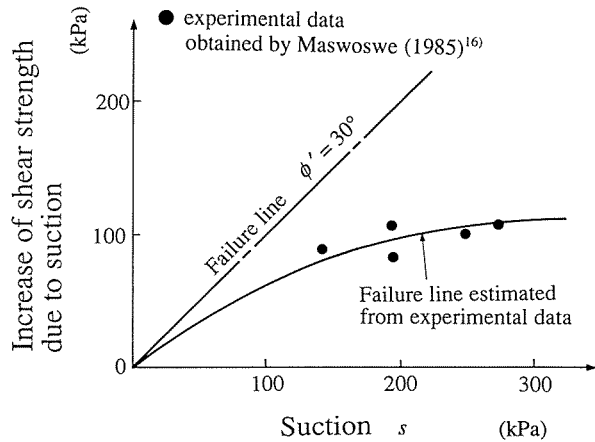


Fig. 2. Increase of shear strength due to suction

$$u_{eq} = u_a - \left(s_e + \frac{s_c - s_e}{s^* + a_e} s^* \right) \quad (s > s_e) \quad (6)$$

Where u_{eq} is the equivalent pore pressure, a_e a material parameter, s_c the critical suction.

The effect of the Point (4) expands the yield surface and increases the resistance to plastic deformation. An increase in suction namely increases both the resistance to the plastic deformation and yield stress (Suction effect (b)). Such an effect can be estimated by formulating the state surface¹⁷⁾ which defines the state boundary of the volume change behavior in unsaturated soils. The state surface can be plotted in the space with the axes, effective mean stress $\log p'$, effective suction s^* , and void ratio e (see Fig. 3). If the relationships between e and $\log p'$ are linear and the $s^* - e$ curves fit into the family of hyperbolic equations, they will be expressed as follows.

$$e = -\lambda^* \log p' + \Gamma^* \quad (7)$$

$$\lambda^* = \frac{\lambda}{1 + y} \quad (8)$$

$$\Gamma^* = \frac{\Gamma + e_0^0 y}{1 + y} \quad (9)$$

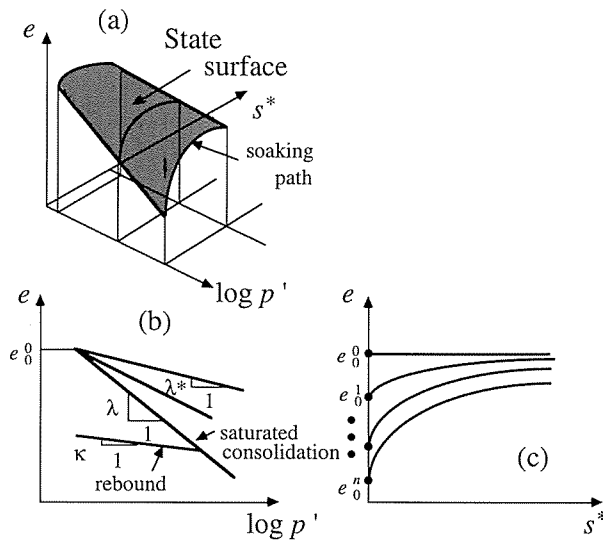


Fig. 3. The generalized state surface

$$y = \left(\frac{s^*}{a_s} \right)^{n_s} \quad (10)$$

$$p' = \frac{1}{3} \sigma'_{ij} \quad (11)$$

Here λ and Γ are respectively λ^* and Γ^* at saturation, λ^* the slope of $e - \log p'$ curves in the plastic range, Γ^* void ratio of a constant $e - \log p'$ curve in plastic range with $p' = \text{unit}$, a_s , n_s and e_0^0 material parameters, σ'_{ij} current effective stress tensor and repeated indices indicate summation.

2) Formulation of normal yield surfaces

In the following chapter, compression stresses are assumed to be negative. The elastoplastic model proposed here, which is generalized in taking account of stress invariant J_3 on the basis of the elastoplastic model proposed by Tanaka²¹⁾, has two yield surfaces, as illustrated in Figs. 4 and 5. One is the Mohr-Coulomb type yield condition which defines the failure surface, that is, the Hvorslev surface. The other is the elliptical cap model with corners which defines the Roscoe surface. Both are connected on the critical state line. The critical state line and these yield surfaces are defined as follows.

$$f = \alpha^*_{cs} I_1 + \frac{\sqrt{J_2}}{g(\theta)} = 0 \quad (12)$$

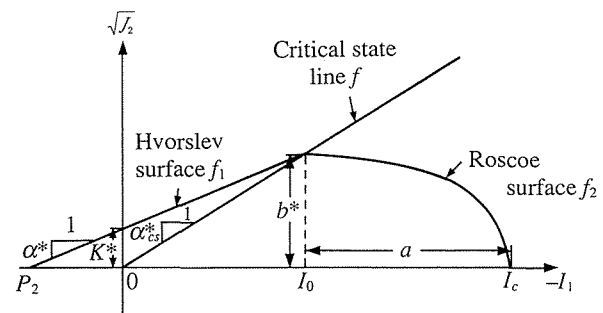


Fig. 4. Yield surfaces of the proposed elastoplastic model at $(-I_1) - \sqrt{J_2}$ section

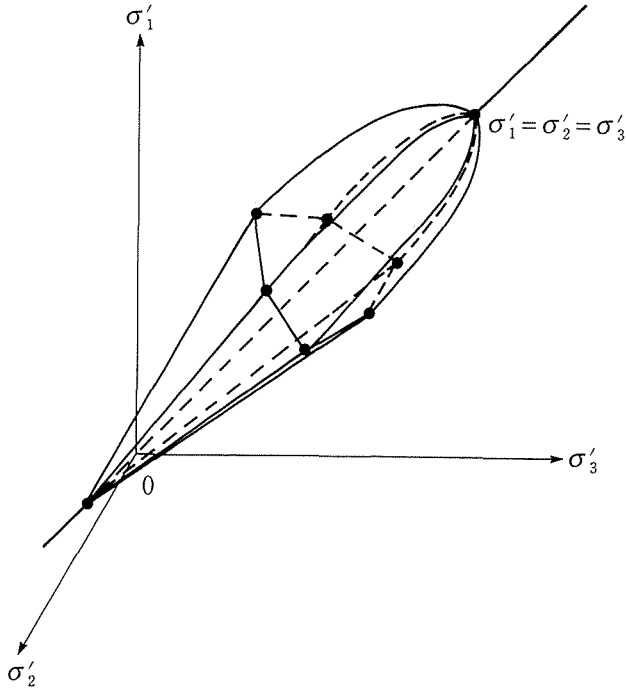


Fig. 5. Yield surfaces of the proposed elastoplastic model in the principal stress space

$$f_1 = \alpha^* I_1 + \frac{\sqrt{J_2}}{g(\theta)} - K^* = 0 \quad (I_0 \leq I_1 \leq P_2) \quad (13)$$

$$f_2 = b^{*2} (I_1 - I_0)^2 + a^2 \frac{J_2}{g(\theta)^2} - a^2 b^{*2} = 0 \quad (I_c \leq I_1 \leq I_0) \quad (14)$$

where θ is the Lode angle, I_1 the first stress invariant, J_2 the second invariant of deviator stress and J_3 the third invariant of deviator stress. They are defined as,

$$I_1 = \sigma'_{ii} \quad (15)$$

$$J_2 = \frac{1}{2} S_{ij} S_{ij} \quad (16)$$

$$J_3 = \frac{1}{3} S_{ij} S_{ik} S_{ki} \quad (17)$$

$$S_{ij} = \sigma'_{ij} - \frac{1}{3} \delta_{ij} I_1 \quad (18)$$

$$\sin 3\theta = \frac{-3\sqrt{3} J_3}{2J_2^{1.5}} \quad (19)$$

where δ_{ij} is the Kronecker delta.

α^{*cs} , α^* , a and b^* are defined in Fig. 4. α^{*cs} , α^* and $g(\theta)$ are expressed as follows.

$$\alpha^{*cs} = \frac{2\sin\phi'_{cs}}{\sqrt{3}(3 - \sin\phi'_{cs})} \quad (20)$$

$$\alpha^* = \frac{2\sin\phi'}{\sqrt{3}(3 - \sin\phi')} \quad (21)$$

$$g(\theta) = \frac{(3 - \sin\phi')}{2(\sqrt{3}\cos\theta - \sin\theta\sin\phi')} \quad (22)$$

where ϕ'_{cs} is the internal friction angle of the critical state line and ϕ' the internal friction angle of the failure line.

K^* , a and b^* relate uniquely to I_0 . They are;

$$K^* = -(\alpha^{*cs} - \alpha^*) I_0 \quad (23)$$

$$a = -(I_c - I_0) \quad (24)$$

$$b^* = -\alpha^{*cs} I_0. \quad (25)$$

I_c can be expressed using I_0 as

$$I_c = (1 + R) I_0 \quad (26)$$

where R is a material parameter, like the aspect ratio. I_0 is the yield stress of this model. If this is an isotropic hardening model with plastic volumetric strain ε_v^p as a hardening parameter, I_c may be estimated based on the state surface concept¹¹⁾.

$$I_c = -3 \exp\left(\frac{B^* - \varepsilon_v^p}{A^*}\right) \quad (27)$$

$$A^* = \frac{(\lambda^* - \kappa)}{2.3(1 + e_0)} \quad (28)$$

$$B^* = \frac{(\lambda^* - \kappa)}{2.3(1 + e_0)} \ln(-p'_0) - \frac{(\Gamma^*_{*0} - \Gamma^*)}{(1 + e_0)} \quad (29)$$

Here, κ is the slope of $e - \log(-p')$ curve at unloading, e_0 the initial void ratio, p'_0 the initial mean effective stress and λ^*_{*0} and Γ^*_{*0} the initial values of λ^* and Γ^* , respectively.

The following two elliptical plastic potential functions are adopted here.

$$\psi_1 = b^2 (I_1 - I_0)^2 + a^{*2} J_2 - a^{*2} b^2 = 0 \quad (I_0 \leq I_1 \leq P_2) \quad (30)$$

$$\psi_2 = b^2 (I_1 - I_0)^2 + a^2 J_2 - a^2 b^2 = 0 \quad (I_0 \leq I_1 \leq P_2) \quad (31)$$

where $a^* = P_2 - I_0$, $b = -\alpha_{cs} I_0$ and α_{cs} is defined to coincide with the Mohr-Coulomb criterion using ϕ'_{cs} as follows²²⁾.

When $\sigma_1 = \sigma_2 > \sigma_3$ (Triaxial compression),

$$\alpha_{cs} = \frac{2 \sin \phi'_{cs}}{\sqrt{3} (3 - \sin \phi'_{cs})} \quad (32)$$

When $\sigma_1 > \sigma_2 = \sigma_3$ (Triaxial extension),

$$\alpha_{cs} = \frac{2 \sin \phi'_{cs}}{\sqrt{3} (3 + \sin \phi'_{cs})} \quad (33)$$

When plane strain condition,

$$\alpha_{cs} = \frac{\tan \phi'_{cs}}{\sqrt{9 + 12 \tan^2 \phi'_{cs}}} \quad (34)$$

The process in which the suction effects are introduced into the elastoplastic model is summarized in Fig. 6. The process is applicable to any elastoplastic models with plastic volumetric strain as a hardening parameter. It is the major advantage of this formulation.

3) Formulation of subloading surfaces

The model proposed here belongs to the category of original subloading surface model⁵⁾. Subloading surfaces are set so as to be similar to the normal yield surfaces (see Fig. 7). The similarity center is assumed to coincide with the origin.

The ratio of the sizes of the subloading surfaces to the normal yield surfaces is expressed as

$$\bar{R} = \frac{\bar{I}_c}{I_c} \quad (0 \leq \bar{R} \leq 1) \quad (35)$$

where \bar{I}_c is the value of I_c on the subloading surfaces and can be estimated based on the assumption that the current stress point is always lying on the subloading surfaces.

A loading criterion is postulated using $\dot{\bar{R}}$ as follows.

$$\begin{aligned} \dot{\bar{R}} > 0 & \quad \text{Loading} \\ \dot{\bar{R}} < 0 & \quad \text{Unloading} \\ \dot{\bar{R}} = 0 & \quad \text{Neutral loading.} \end{aligned} \quad (36)$$

Here, $\dot{\bar{R}}$ is an increment of \bar{R} .

We specify the conjugate point on the normal yield surfaces with the same outer normal direction as the current stress point σ'_{ij} on the subloading surfaces. Then, the conjugate effective stress tensor $\hat{\sigma}'_{ij}$ is

$$\hat{\sigma}'_{ij} = \frac{\sigma'_{ij}}{\bar{R}} \quad (37)$$

The hardening modulus H is postulated as

$$H = \hat{H} + (h - \hat{H})(1 - \bar{R}^*)^{\alpha_h} \quad (38)$$

$$\bar{R}^* = \frac{\bar{R} - \bar{R}_i}{1 - \bar{R}_i} \quad (39)$$

where \hat{H} is the hardening modulus at the conjugate point, h an arbitrary constant which

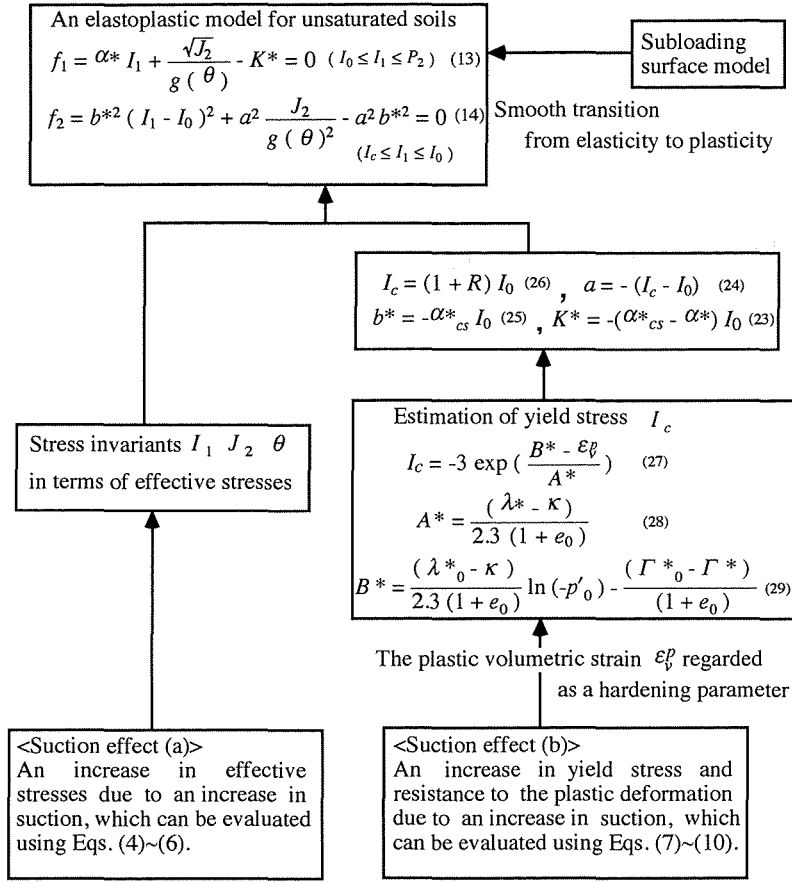
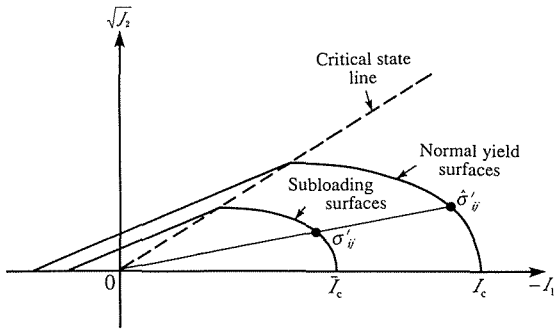


Fig. 6. Suction effects and their introduction into the elastoplastic model


 Fig. 7. Normal yield and subloading surface at $(-I_1) - \sqrt{J_2}$ section

estimated on the basis of the generalized plasticity theory³⁾. The effective stress increment $\dot{\sigma}'_{ij}$ is given by

$$\dot{\sigma}'_{ij} = D_{ijkl} (\dot{\varepsilon}_{ij} - \dot{\varepsilon}_{ij}^p) \quad (40)$$

where D_{ijkl} is the elastic modulus tensor, $\dot{\varepsilon}_{ij}$ the strain increment tensor and $\dot{\varepsilon}_{ij}^p$ the plastic strain increment tensor.

If plastic deformation occurs, the plastic strain increment $\dot{\varepsilon}_{ij}^p$ is assumed to be given as

$$\dot{\varepsilon}_{ij}^p = \langle L \rangle \bar{n}_{ij} \quad (41)$$

where L is the loading function and it is determined by

$$L = \frac{n_{kl} D_{klmn} \dot{\varepsilon}_{mn}}{H + D_{abcd} n_{ab} \bar{n}_{cd}} \quad (42)$$

4) Procedure for estimation of stress and strain on subloading surfaces

The stress and plastic strain increments are

satisfies the condition $h \gg H$, α_h a material parameter and \bar{R}_i the initial value of \bar{R} along a loading process.

Here, n_{ij} and \bar{n}_{ij} are, respectively, the unit tensor of plastic loading and unit gradient tensor of plastic potential at the conjugate point. They are defined as follows.

$$n_{ij} = \frac{\frac{\partial f}{\partial \hat{\sigma}'_{ij}}}{\left[\left[\frac{\partial f}{\partial \hat{\sigma}'_{kl}} \right] \left[\frac{\partial f}{\partial \hat{\sigma}'_{kl}} \right] \right]^{1/2}} \quad (43)$$

$$\bar{n}_{ij} = \frac{\frac{\partial \psi}{\partial \hat{\sigma}'_{ij}}}{\left[\left[\frac{\partial \psi}{\partial \hat{\sigma}'_{kl}} \right] \left[\frac{\partial \psi}{\partial \hat{\sigma}'_{kl}} \right] \right]^{1/2}} \quad (43)$$

Here, f and ψ denote, respectively, yield and plastic potential functions.

Consolidation Analysis Method for Unsaturated Soils

1) Field equations and FEM formulation

In many soil mechanics problems, it can be assumed that pore air is always connected with the atmosphere and the permeability for the air flow is sufficiently high. Pore air pressure would be the same as the atmospheric pressure. Considering that the pore air pressure is not the pressure of air bubbles but the air pressure surrounding soil particles at the boundary which is the atmospheric pressure, the assumption can be applied for insular air saturation. In the case of insular air saturation, the pressure of air bubbles is assumed to be the same as the pore water pressure. If these assumptions are valid, the field equations for consolidation problems can be represented by the following two equations.

$$\sigma'_{ij,j} + \delta_{ij} u_{eq,i} + \gamma F_i = 0 \quad (45)$$

$$q_{i,i} - \dot{a}_{ii} + S_r \dot{\epsilon}_{ii} = 0 \quad (46)$$

Equation (45) is the equilibrium equation of soil and Eq. (46) is the Richards' mass conservation equation of pore water. Here, γ is the

unit weight of soil, F_i the components of body force vector, q_i the components of relative displacement velocity vector of water with respect to soil skeleton, a_{ii} the change of storage of water due to the change of the degree of saturation S_r , ϵ_{ii} the volumetric strain of soil skeleton. Subscripts after a comma denote spatial differentiation. A superposed dot denotes differentiation with respect to time.

If the field equations are introduced to the discrete system using the finite element method and the solution procedure based on the modified Newton-Raphson method is adopted¹⁵⁾, they will be;

$$\delta_{m+1} = \delta_m + \Delta \delta_{m+1} \quad (47)$$

$$\Delta \delta_{m+1} = -\mathbf{K}_0^* \Phi_m \quad (48)$$

where δ is the unknown vector, Φ the residual vector and \mathbf{K}_0^* the coefficient matrix. They are obtained as follows.

$$\Delta \delta = \begin{Bmatrix} \Delta u(t_n) \\ \Delta u_w(t_n) \end{Bmatrix}, \quad \Phi_m = \begin{Bmatrix} \Phi_m^1 \\ \Phi_m^2 \end{Bmatrix} \quad (49)$$

$$\mathbf{K}_0^* = \begin{bmatrix} \mathbf{K} & \mathbf{L} \\ \mathbf{L}^T & -\alpha \Delta t \bar{\mathbf{K}} - \mathbf{E} \end{bmatrix} \quad (50)$$

$$\mathbf{K} = \sum_{i=1}^l \int_V \mathbf{B}^T \mathbf{D} \mathbf{B} dV, \quad \mathbf{L} = \sum_{i=1}^l \int_V \mathbf{C}^T \mathbf{N} dV \quad (51)$$

$$\bar{\mathbf{K}} = \sum_{i=1}^l \int_V \mathbf{N}^T \mathbf{R} \mathbf{N}' / \gamma_w dV, \quad \mathbf{E} = \sum_{i=1}^l \int_V \mathbf{N}^T \mathbf{N} / E' dV \quad (52)$$

$$\Phi_m^1 = \sum_{i=1}^l \int_V \mathbf{B}^T \sigma'(t_n)_m dV + \sum_{i=1}^l \int_V \mathbf{C}^T u_{eq}(t_n)_m dV \\ - \sum_{i=1}^l \int_{S_3} \mathbf{N}_{ub}^T \mathbf{N}_{ub} T_b(t_n) dS - \sum_{i=1}^l \int_V \gamma \mathbf{N}_u^T \mathbf{F}(t_n) dV \quad (53)$$

$$\Phi_m^2 = \sum_{i=1}^l \int_V \mathbf{S}_r \mathbf{N}^T \mathbf{C} u(t_n)_m dV \\ - \sum_{i=1}^l \int_V \mathbf{S}_r \mathbf{N}^T \mathbf{C} u(t_{n-1})_m dV$$

$$\begin{aligned}
 & -\sum_{i=1}^l \int_V \mathbf{N}^T \mathbf{a}(t_n)_m dV + \sum_{i=1}^l \int_V \mathbf{N}^T \mathbf{a}(t_{n-1}) dV \\
 & + \Delta t \cdot \alpha \sum_{i=1}^l \int_{S_4} \mathbf{N}_b^T \mathbf{N}_b Q_b(t_n) dS \\
 & + \Delta t \cdot (1-\alpha) \sum_{i=1}^l \int_{S_4} \mathbf{N}_b^T \mathbf{N}_b Q_b(t_{n-1}) dS \\
 & - \Delta t \cdot \alpha \sum_{i=1}^l \int_V \mathbf{N}^T \mathbf{T} \mathbf{q}_p(t_n)_m dV \\
 & - \Delta t \cdot \alpha \sum_{i=1}^l \int_V \mathbf{N}^T \mathbf{T} \mathbf{q}_g(t_n)_m dV \\
 & - \Delta t \cdot (1-\alpha) \sum_{i=1}^l \int_V \mathbf{N}^T \mathbf{T} \mathbf{q}_p(t_{n-1}) dV \\
 & - \Delta t \cdot (1-\alpha) \sum_{i=1}^l \int_V \mathbf{N}^T \mathbf{T} \mathbf{q}_g(t_{n-1}) dV
 \end{aligned} \tag{54}$$

where $\boldsymbol{\sigma}'$ is the effective stress vector, u the nodal displacement vector, u_w the nodal pore water pressure, \mathbf{N} the interpolation function for pore water pressure, \mathbf{N}' the gradient matrix for pore water pressure, \mathbf{N}_u the interpolation function for displacement, \mathbf{B} the nodal displacement - strain matrix, \mathbf{C} the nodal displacement - volumetric strain matrix, \mathbf{D} the elasticity matrix, \mathbf{R} the permeability matrix, \mathbf{F} the body force vector, \mathbf{a} the change of storage of water due to the change of the degree of saturation, \mathbf{T}_b the prescribed traction on the boundary nodal points, Q_b the prescribed flux on the boundary nodal points, \mathbf{q} the flux vector, $E'_f = E_f/n$, $E_f = \partial S_r / \partial s$, n : porosity, α the coefficient characterizing single-step temporal discretization. Superscript T denotes the transposition of matrix and subscripts b , p , g , m and n denote the value on the boundary, the value due to pore water pressure, the value due to gravitational potential, the number of iterations and number of time steps, respectively.

The operations of Eqs. (47), (48), (53) and (54) should be iterated until the solutions of $\boldsymbol{\delta}$ have been satisfied with the convergence criteria for which the second norm of $\boldsymbol{\delta}$ was used here.

The operations of plastic stress calculation were also inserted between Eqs. (48) and (53).

The calculation of plastic stresses on the subloading yield surfaces was performed in terms of the generalized plasticity theory described in section 4) in the second chapter. The calculation of plastic stresses on the normal yield surfaces was conducted in terms of the return mapping algorithm²⁰⁾, because the calculated stress point must always lie on the yield surface in the calculation of the plastic stresses on the normal yield surfaces. The return mapping algorithm is schematically shown in Fig. 8. In this procedure, first the stresses are predicted using elastic relations, next the relaxation of stresses is iteratively carried out and then the final stresses which are consistent with those at a point on the yield surface are calculated. The process is shown in Table 2.

2) Soil water retention and permeability properties

Material nonlinear properties need to be taken into account to conduct consolidation analysis. We considered nonlinear properties of stress - strain relationship, permeability and soil water retention. The elastoplastic model with the two suction effects described above was employed as the stress - strain relationship.

It is reasonable to assume that soil water retention curves may not change appreciably with the deformation of soil¹³⁾. The following equations

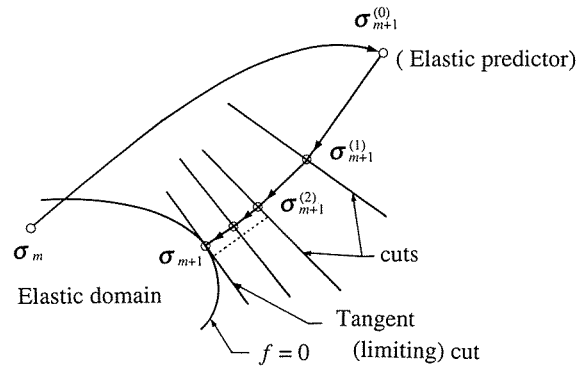


Fig. 8. Numerical implementation of the generalized return mapping algorithm (after Ortiz & Simo (1986)²⁰⁾)

Table 2. Calculation procedure of generalized return mapping algorithm

(1) Total strain update :

$$\boldsymbol{\varepsilon}_{m+1} = \boldsymbol{\varepsilon}_m + \Delta \boldsymbol{\varepsilon}_{m+1}$$

$$\Delta \boldsymbol{\varepsilon}_{m+1} = \mathbf{B} \Delta \boldsymbol{\delta}_{m+1}$$

(2) Elastic predictor :

$$\Delta \boldsymbol{\sigma}_{m+1}^e = \mathbf{D}_m \Delta \boldsymbol{\varepsilon}_{m+1}$$

$$\boldsymbol{\sigma}_{m+1}^{(0)} = \boldsymbol{\sigma}_m + \Delta \boldsymbol{\sigma}_{m+1}^e$$

(3) Check for yielding :

$$f_{m+1}^{(0)} = f(\boldsymbol{\sigma}_{m+1}^{(0)}) \leq 0 ?$$

$$\text{YES : } \quad \boldsymbol{\sigma}_{m+1} = \boldsymbol{\sigma}_{m+1}^{(0)} \quad \text{EXIT}$$

$$\text{NO : } \quad i = 0$$

(4) Plastic correctors :

$$\lambda = f_{m+1}^{(i)} / \left\{ \left(\partial f_{m+1}^{(i)} / \partial \boldsymbol{\sigma} \right)^T \mathbf{D}_{m+1}^{(i)} \left(\partial \psi_{m+1}^{(i)} / \partial \boldsymbol{\sigma} \right) - \left(\partial f_{m+1}^{(i)} / \partial \boldsymbol{\varepsilon}^p \right)^T \left(\partial \psi_{m+1}^{(i)} / \partial \boldsymbol{\sigma} \right) \right\}$$

$$\boldsymbol{\sigma}_{m+1}^{(i+1)} = \boldsymbol{\sigma}_{m+1}^{(i)} - \lambda \mathbf{D}_{m+1}^{(i)} \left(\partial \psi_{m+1}^{(i)} / \partial \boldsymbol{\sigma} \right)$$

$$\boldsymbol{\varepsilon}_{m+1}^{p(i+1)} = \boldsymbol{\varepsilon}_{m+1}^{p(i)} + \lambda \left(\partial \psi_{m+1}^{(i)} / \partial \boldsymbol{\sigma} \right)$$

(5) Convergence check :

$$\left| f_{m+1}^{(i+1)} \right| \leq \text{TOL} \left| f_{m+1}^{(0)} \right| ?$$

$$\text{YES : } \quad \boldsymbol{\sigma}_{m+1} = \boldsymbol{\sigma}_{m+1}^{(i+1)}, \quad \boldsymbol{\varepsilon}_{m+1}^p = \boldsymbol{\varepsilon}_{m+1}^{p(i+1)}$$

$$\text{NO : } \quad i \leftarrow i + 1 \quad \text{GO TO (4)}$$

may therefore be considered to express the soil water retention curves. The equations were formulated by guaranteeing the continuity of the tangential slope $c (= 1/E_f)$ of the soil water retention curve. The model is therefore designated here as the Tangential model.

$$c = - (1 - S_{re} + h_s S_{re}) \frac{(P_a - s_e)}{(P_a - s)^2} \quad (s \leq s_e) \quad (55)$$

$$c = (H_c) \left[c_e + \left\{ \frac{s - s_e}{s_m - s_e} \right\}^{m_r} (c_m - c_e) \right] + (1 - H_c) \left[c_f + \left\{ \frac{s - s_f}{s_m - s_f} \right\}^{n_r} (c_m - c_f) \right] \quad (s_e < s < s_f) \quad (56)$$

$$c = c_f \quad (s \geq s_f) \quad (57)$$

where P_a is the atmospheric pressure, S_{re} the degree of saturation of air entry, h_s Henry's coefficient of solubility, $H_c=1$ at $s \leq s_m$ or $H_c=0$ at $s > s_m$ and subscripts m and f denote respectively the values at the points F and M shown in Fig. 9. Point F is the lowest suction point among the points where the tangential slope is almost constant in the range of greater suction and point M is the point where the tangential slope is maximum. The parameters m_r and n_r are obtained as follows using the continuity condition of the value c .

$$m_r = \frac{c_m(s_m - s_e) - (S_{re} - S_{rm})}{(S_{re} - S_{rm}) - c_e(s_m - s_e)} \quad (58)$$

$$n_r = \frac{c_m(s_m - s_f) - (S_{rf} - S_{rm})}{(S_{rf} - S_{rm}) - c_f(s_m - s_f)} \quad (59)$$

The permeability is considerably influenced by the deformation and the change of the degree of saturation of soil. Then, the permeability property was assumed to be a function of e and S_r as follows.

$$k = k_s E_p H_p \quad (60)$$

$$E_p = \frac{1+e_0}{1+e} \left(\frac{e}{e_0} \right)^{n_p} \quad (61)$$

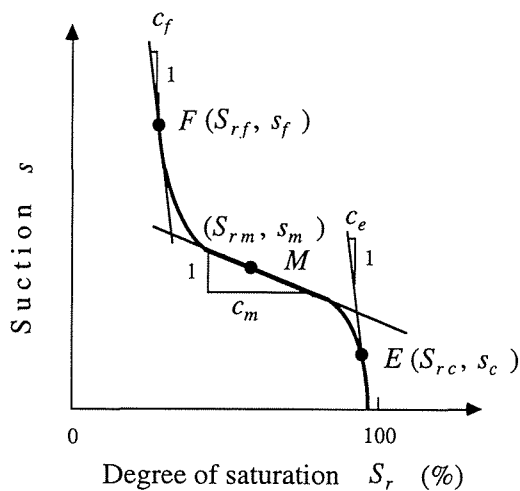


Fig. 9. The tangential model for soil water retention curves

$$H_p = \left[\frac{S_r - S_{rf}}{S_{re} - S_{rf}} \right]^{m_p} \quad (62)$$

Here k_s is the permeability at saturation, m_p and n_p are material parameters.

Analyses of Saturated Collapse Behavior

1) K_0 consolidation test simulations

Here, K_0 consolidation test series with and without soaking were simulated using the consolidation analysis method described above. The experimental data of Lower Cromer Till (a low plastic clay, $I_p=13$, $w_L=25\%$, $\rho_s = 2.69$) were obtained by Maswoswe¹⁶⁾. The grading curve of Lower Cromer Till is shown in Fig.10. Table 3 presents the material parameters. The water retention curve is shown in Fig. 11. Here, the bulk and shear moduli are assumed to be functions of p' and $\sqrt{J_2}$ as follows.

$$K = \frac{-2.3(1+e_0)}{\kappa} p' + K_i \quad (63)$$

$$G = G_i + \gamma_j \sqrt{J_2} - \gamma_p p' \quad (64)$$

where K and G are the bulk and shear moduli, respectively. G_i and K_i , γ_j are γ_p material parameters.

These material parameters shown in Table 3 were derived as follows. The air entry suction s_e was obtained from the soil water retention curve shown in Fig. 11. The material parameters s_e and a_e concerned with effective stress can be determined as follows from the shear strength data at the wet side of critical state¹⁴⁾. From the shear strength data, if the shear failure occurs on the failure line, we can obtain the u_{eq} values as the distances of the horizontal axis between the failure points on

$\frac{(\sigma_1 - \sigma_3)}{2} - \left\{ \frac{(\sigma_1 + \sigma_3)}{2} - u_a \right\}$ stress paths and the

points with the same shear strength $\frac{(\sigma_1 - \sigma_3)_f}{2}$ on

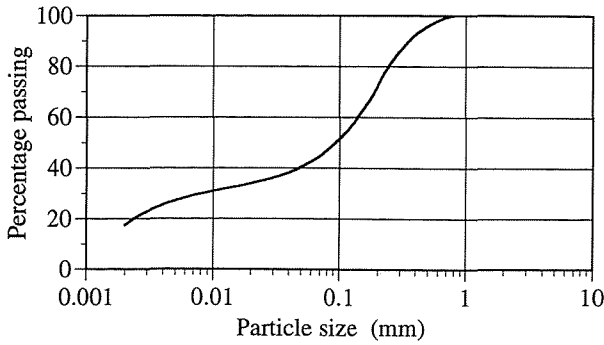


Fig. 10. Grading curve for Lower Cromer Till

Table 3. Material parameters of Lower Cromer Till used in the analyses

Elasticity	$\kappa = 0.035, K_i = G_i = 0 \text{ kPa}, \gamma_j = 0.0, \gamma_p = 118.6$
Subloading	$h = 2 \times 10^5 \text{ kPa}, \alpha_h = 4.8$
Plasticity	$\phi' = 28^\circ, \phi'_{cs} = 30^\circ, R = 0.42,$ $I_c = -1050 \text{ kPa}, p'_0 = -280 \text{ kPa}$
Effective stress	$s_c = 162.5 \text{ kPa}, a_e = 162.5 \text{ kPa},$ $s_e = 0 \text{ kPa}$
State surface	$\lambda = 0.166, \Gamma = 0.840, e_0^0 = 1.087,$ $a_s = 360.5 \text{ kPa}, n_s = 1.528$
Initial condition	$S_{r0} = 0.45, s_0 = 240 \text{ kPa},$ $e_0 = 0.661, \gamma = 17.63 \text{ kN/m}^3$
Permeability and Soil water retention	$k_s = 1 \times 10^{-2} \text{ m/d}, m_p = 3.0, n_p = 3.0,$ $h_s = 0.02, \gamma_w = 10 \text{ kN/m}^3, P_a = -100 \text{ kPa},$ $S_{re} = 0.96, S_{rm} = 0.95, S_{rf} = 0.45, s_m = 0.1 \text{ kPa},$ $s_f = 240 \text{ kPa}, c_m = 3.8 \times 10^{-3}, c_f = 7.5 \times 10^{-4}$

the failure line. Once we can get u_{eq} values, s_e and a_e can be estimated from the linear relationship between s^* and s^*/f , where $f = u_{eq} - u_a + s_e$, using the least square method. Next, the material parameters $\lambda, \Gamma, e_0^0, a_s$ and n_s concerned with the state surface can be obtained as follows. The parameters λ and Γ can be estimated from the relationship between e and $\log p'$ under saturation conditions. Using the $e - \log p'$ relationships as shown in Fig. 3 (b), e_0^0 , and λ^* values for each s^* value can be obtained. As the values of y can be estimated from Eq. (8) and the relationship between $\log y$ and $\log s^*$ from Eq. (10) is linear, we

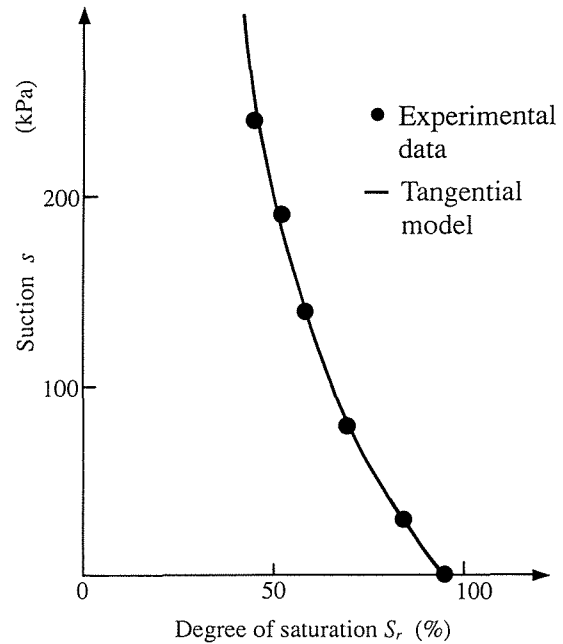
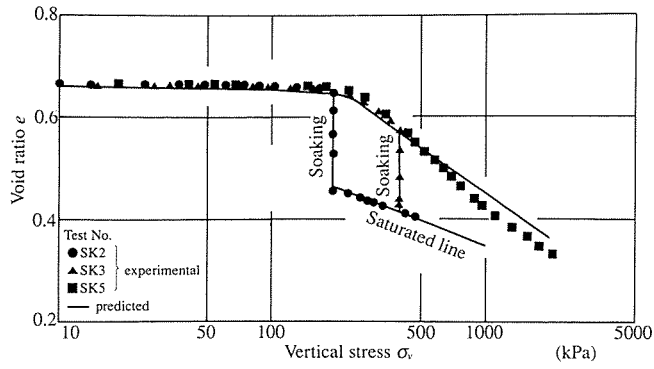


Fig. 11. Soil water retention curve of Lower Cromer Till

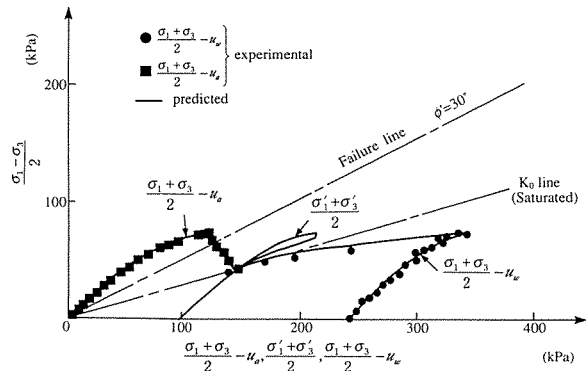
can obtain a_s and n_s using the least square method. Other parameters concerned with the elastic and plastic properties could be estimated from experimental data obtained by triaxial shear and consolidation tests except for R, h and α_h . The value of parameter h concerned with subloading surface employed the value usually used. The parameters R and α_h were estimated from the trial and error numerical simulations.

The results of these simulations are shown in Fig. 12. Here, the effective stresses are those estimated using Eqs. (4) ~ (6)

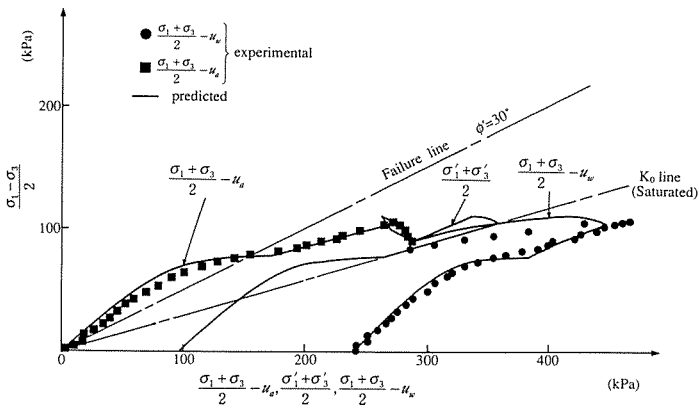
Figure 12-(a) shows the $e - \log \sigma_v$ relationships for the K_0 consolidation test simulations. The results in the K_0 consolidation process become asymptotic to the saturation line as σ_v increases. This is ascribed to the fact that the compression of the soil skeleton with the increase of σ_v results in the higher degree of saturation. In the soaking processes, a great volume decrease (the saturation collapse phenomenon) is induced and the points after soaking are almost located on the saturation line. Simulation results are consistent with the identical test results.



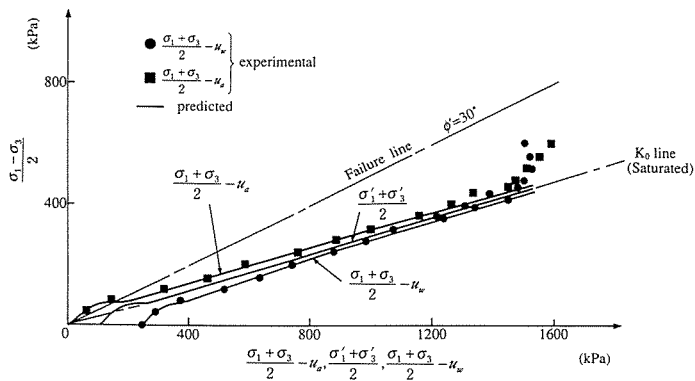
(a)



(b)



(c)



(d)

Fig. 12. K_0 consolidation simulation results on Lower Cromer Till
 (a) Relationship between void ratio and vertical stress
 (b) Stress paths with soaking (SK2) (c) Stress paths with soaking (SK3) (d) Stress paths without soaking (SK5)

Figures. 12-(b) ~ (d) show the associated stress paths. Figures. 12-(b) and (c) represent the K_0 stress paths with soaking and Fig. 12-(d) represents those without soaking. During soaking, the values of deviator stress decrease. The stress points after soaking lie almost on the saturation K_0 line. The effective stress paths trace on the saturation K_0 lines. Thus, it was found that this consolidation analysis method enabled to estimate the saturation collapse behavior measured in the laboratory tests.

2) The seepage model test simulation

A seepage model test simulation on the loosely compacted DL clay (a non-plastic silt, $\rho_s = 2.65$) samples was performed using the consolidation analysis method described above. The grading curve of DL clay is shown in Fig.13. The seepage test was performed to simulate the process of seepage of fill-type dams. The components of the test apparatus used here are shown in Fig. 14 and Photo 1. The dimensions of the soil-container box used here were as follows: height $H = 50.5$ cm, width $W = 30$ cm and length $L = 120$ cm. The box had two loading systems with which back air pressure up to 200 kPa and vertical stress up to 300 kPa could be separately applied to soil models. The front surface of the box was covered with a transparent acrylic resin board. The water tanks were also prepared on both sides of the box to conduct seepage. The DL clay

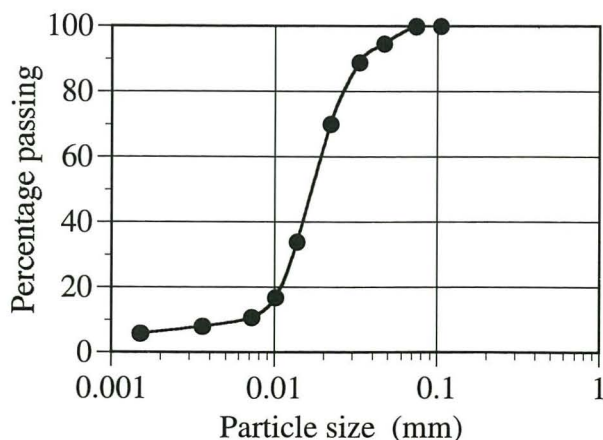


Fig. 13. Grading curve for DL clay

material with water content $w = 17\%$ was statically compacted in the box so that the dry density ρ_d was 1.30 and the height, width and length of the model were 45, 30, 100 cm, respectively. Under these conditions, the initial void ratio e_0 , initial degree of saturation $S_{r,0}$ and initial suction s_0 were 1.05, 45% and 30 kPa, respectively. Pore water pressures and displacements were measured during the test. The pore water pressures were measured using the pore water pressure transducers placed at prescribed points in the model. The displacements were obtained from the amount of movements of the grids for which pictures were taken. The grids were printed on the rubber membranes which were put on the greased acrylic board. The procedure of the test was as follows. First, the back air pressure of 98 kPa was applied to the whole soil model in order to shift the pore water pressures to positive values. The soil model was

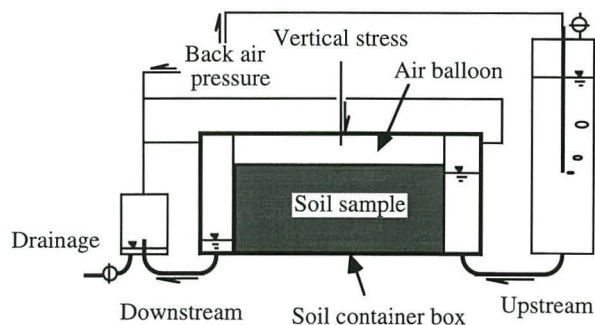


Fig. 14. The components of seepage test apparatus



Photo 1. The seepage test apparatus

consolidated by applying the 147 kPa vertical stress after the pore water pressures became constant. After completing the consolidation, the water levels of upstream and downstream sides were, respectively, raised to 37.5 cm and 2.3 cm in order to perform the seepage test.

The processes of construction of the model, consolidation due to vertical stress and seepage were simulated using the consolidation analysis method. The finite element mesh and boundary conditions used are shown in Fig. 15. The elements used here were quadratic isoparametric for the displacement field and superparametric for the pore water field. Reduced integration (a 2x2 Gauss point integration) was also adopted. The identified parameters are shown in Table 4. The results of the simulation concerned with distributions of suction and displacement during seepage are shown in Figs. 16 and 17 with experimental results. Figure 16 illustrates the distribution of suction. The values of suction induced in the model were high just before the commencement of seepage. The suction distribution of the simulation was similar to that of the hydrostatic pressure, while the distribution in the test was more complex, presumably due to the initial non-uniformity. The values of suction became lower as seepage went on. The suction distribution in both test and simulation at $t = 150$ and 300 minutes was very similar. The suction values increased toward the upper corner of the

downstream side and the maximum suction value was observed near the upper corner of the downstream side. At the steady state, the values of suction became low. The suction distribution in the simulation was consistent with that of the test.

Figure 17 shows the distribution of displacement. The distribution of displacement at $t = 0$ minute shows the state just after consolidation. The amount of displacement due to vertical stress was very small as in the state at $t = 0$ minute. When seepage started, the deformation progressed from the upstream side. The deformation was

Table 4. Material parameters of DL clay used in the seepage test simulation

Elasticity	$\kappa = 0.010, K_i = G_i = 0 \text{ kPa}, \gamma_j = -40.4, \gamma_p = 70.0$
Subloading	$h = 2 \times 10^5 \text{ kPa}, \alpha_h = 2.0$
Plasticity	$\phi' = 26.2^\circ, \phi'_{cs} = 32.2^\circ, R = 1.2,$ $l_c = -510 \text{ kPa}, p'_0 = -147 \text{ kPa}$
Effective stress	$s_c = 43.0 \text{ kPa}, a_e = 33.3 \text{ kPa},$ $s_e = 10 \text{ kPa}$
State surface	$\lambda = 0.143, \Gamma = 1.310, e_0^0 = 1.638,$ $a_s = 135,900 \text{ kPa}, n_s = 0.280$
Initial condition	$S_{r0} = 0.45, s_0 = 30 \text{ kPa},$ $e_0 = 1.050, \gamma = 14.7 \text{ kN/m}^3$
Permeability and Soil water retention	$k_s = 6 \times 10^{-5} \text{ m/d}, m_p = 3.68, n_p = 3.0,$ $h_s = 0.02, \gamma_w = 9.8 \text{ kN/m}^3, P_a = -98 \text{ kPa},$ $S_{re} = 0.99, S_{rm} = 0.60, S_{rf} = 0.16, s_m = 13 \text{ kPa},$ $s_f = 120 \text{ kPa}, c_m = 1 \times 10^{-2}, c_f = 9 \times 10^{-4}$

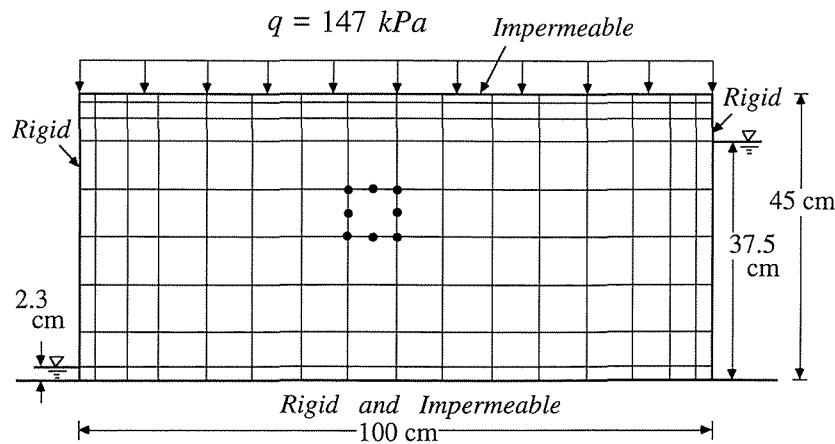


Fig. 15. Finite element mesh and boundary conditions for the seepage test simulation

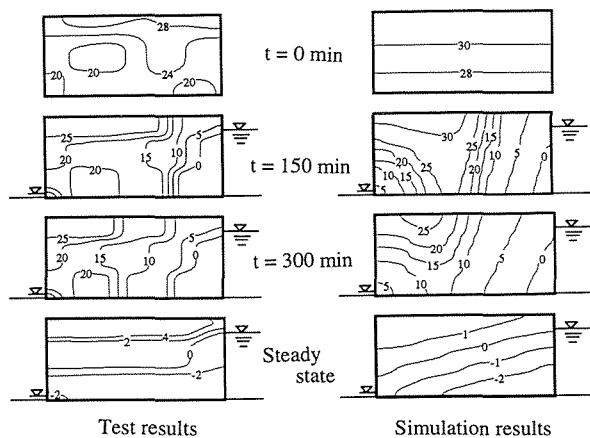


Fig. 16. Suction distributions during seepage (unit=kPa)

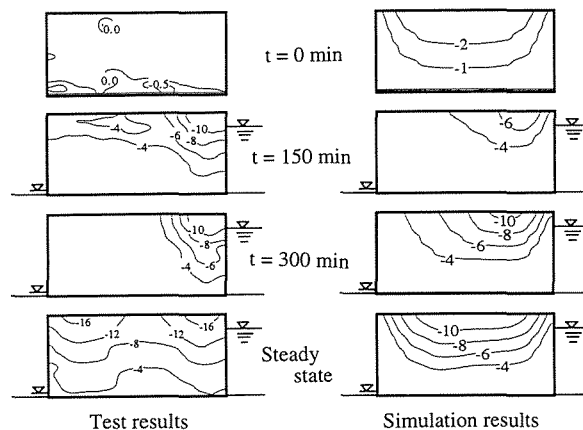


Fig. 17. Vertical displacement distributions during seepage (unit=mm)

induced by saturation collapse. The displacement distribution in both test and simulation at $t = 150, 300$ minutes and steady state was very similar. Though the amount of displacement in the simulation was slightly smaller than that of the test, both were comparatively consistent as a whole. Thus, the deformation behavior concerned with saturation collapse could be estimated using the consolidation analysis method described above.

3) Analysis of an earth-fill dam during reservoir filling

The behavior of a virtual earth dam constructed with a collapsible soil (Lower Cromer Till) during reservoir filling was analyzed here using the consolidation analysis method. The dimensions of the dam ($H = 50$ m, $B = 305$ m), finite element mesh, the speed of construction and the boundary conditions are shown in Fig. 18. As

boundary conditions, the pore water pressure was zero at the downstream foundation and the base was rigid and impervious. The elements used here was the same as those in the previous analyses. Reduced integration (a 2×2 Gauss point integration) was also adopted. The reservoir was filled in 270 days at a constant rate and the water level was 45 m. The material parameters and the retention curve based on the experimental data for Lower Cromer Till are presented in Table 3 and Fig. 11, respectively.

The results of this analysis are shown in Figs. 19~23. Figure 19 shows the deformation at each stage. The deformation advanced as the saturation zone expanded. At the completion of construction, settlement was at maximum at the center of the embankment, as seen in the typical measurement records, and horizontal displacements were still small. The degree of safety of this embankment

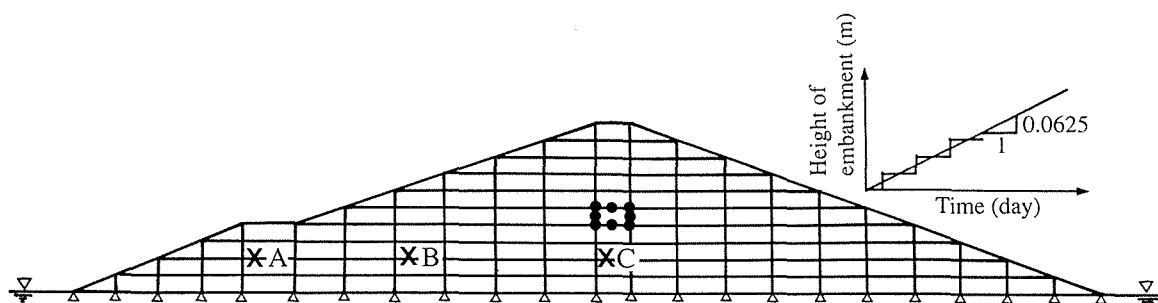


Fig. 18. Finite element mesh and boundary conditions

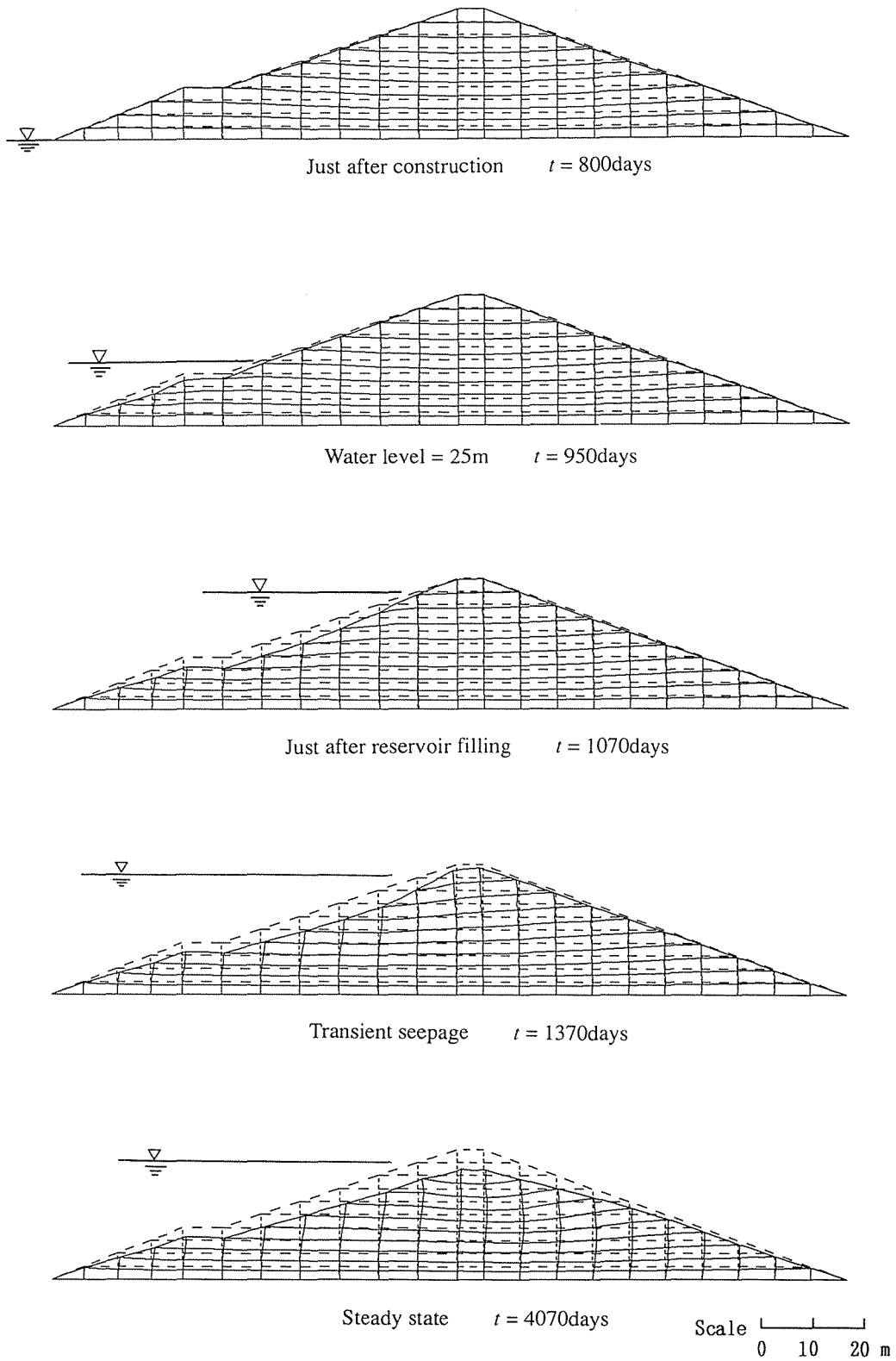


Fig. 19-(a)

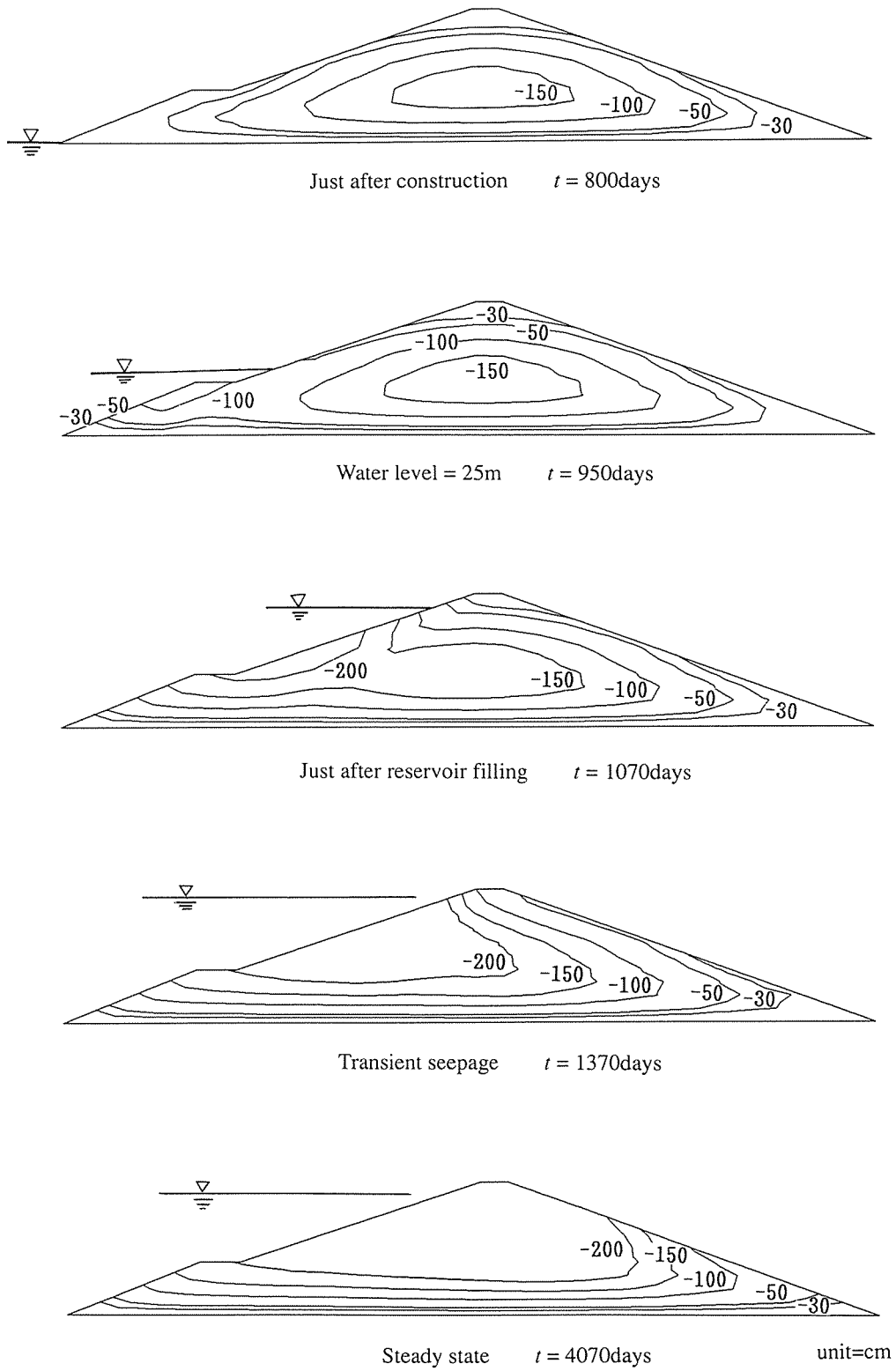


Fig. 19-(b)

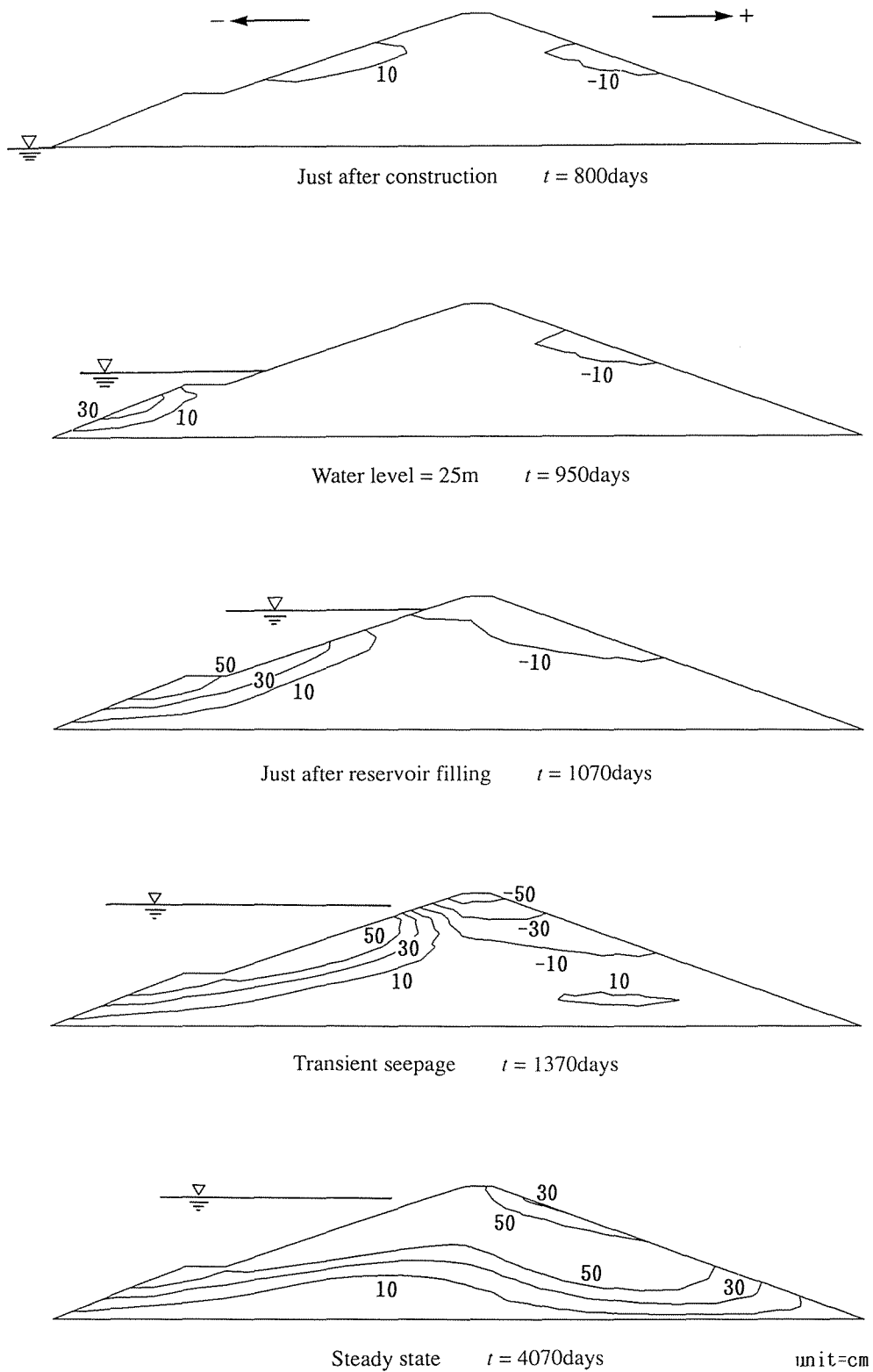


Fig. 19-(c)

Fig. 19. The analysis results (deformation) of an earth-fill dam at each stage (a) Deformation (b) Vertical displacement (c) Horizontal displacement

was thus very high. The positive values of the horizontal displacement were associated with the downstream direction. During the filling of the reservoir, the water-load on the upstream slope caused downstream and downward movements, and the collapse due to wetting caused downward movement and upstream rotation of the embankment. These phenomenon coincided with the effects of reservoir filling pointed out by Nobari and Duncan¹⁹. As a result, the upstream slope of the embankment below the water deformed toward the downstream side, and near the crest it deformed in the opposite direction, toward the upstream side. Tension cracks may therefore be induced on the downstream slope near the crest. In the steady state, settlement was remarkably large and the maximum value reached about 4m. The free board was not, therefore, sufficient in this case.

Figure 20 shows the change of horizontal displacements with time at the upstream crest. The dam showed an upstream deformation just after the commencement of seepage and then moved back downstream. This behavior is consistent with the typical dam behavior during reservoir filling and it could not be analyzed until the consolidation analysis method taking into

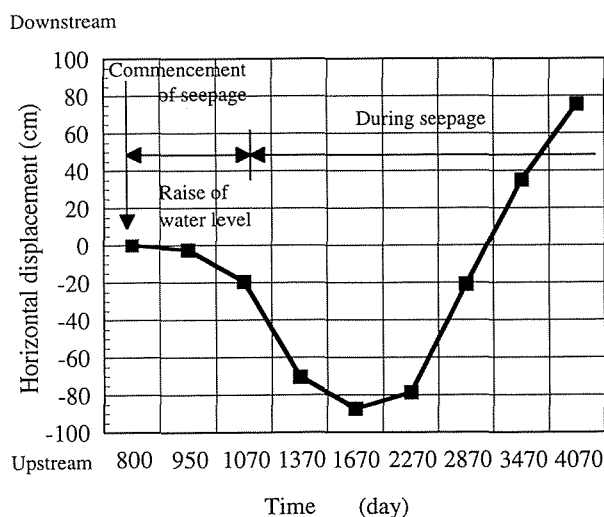


Fig. 20. The time change of horizontal displacement at the upstream crest

account the saturation collapse was adopted.

Figure 21 shows the distribution of shear strain. The shear strain also increased as the water level went up. At a high water level, the maximum value of shear strain reached about 8%. The shear strains were concentrated near the upstream slope. However, this embankment was still safe, since the shear strength magnitude of the fill material at saturation was sufficiently high.

Figures 22-(a) and (b) illustrate the distribution of the vertical stress and pore water pressure, respectively. The compression pressure was assumed to be negative. At the construction stage, a large amount of suction occurred. The suction induced a great deal of vertical stress. The saturation zone gradually expanded as the water level went up. The vertical stress decreased with the expansion of the saturation zone.

Figure 23 shows the $e - \log p$ or $e - \log p'$ curves at A, B and C points in the embankment illustrated in Fig. 18. The open circles represent the results of the isotropic compression test of Lower Cromer Till. The $e - \log p$ curves at A, B and C in the construction stage traced on the same line which was almost consistent with the line estimated from the experimental data. During reservoir filling, the decrease of void ratio due to the decrease in suction could be observed and when the suction became less than s_e the points lay on the saturation $e - \log p'$ line. During the process of seepage, the $e - \log p'$ curves at A and B were in the elastic region and under the unloading process. The unloading process was induced by buoyant uplift forces, that is, a decrease in effective stresses due to an increase in pore water pressure.

Conclusions

We described the consolidation analysis method with an elastoplastic constitutive model for unsaturated soils. The model included two suction effects which were related to increases in effective stresses, yield stress and resistance to the plastic deformation due to an increase in suction. The smooth transition from elasticity to plasticity was

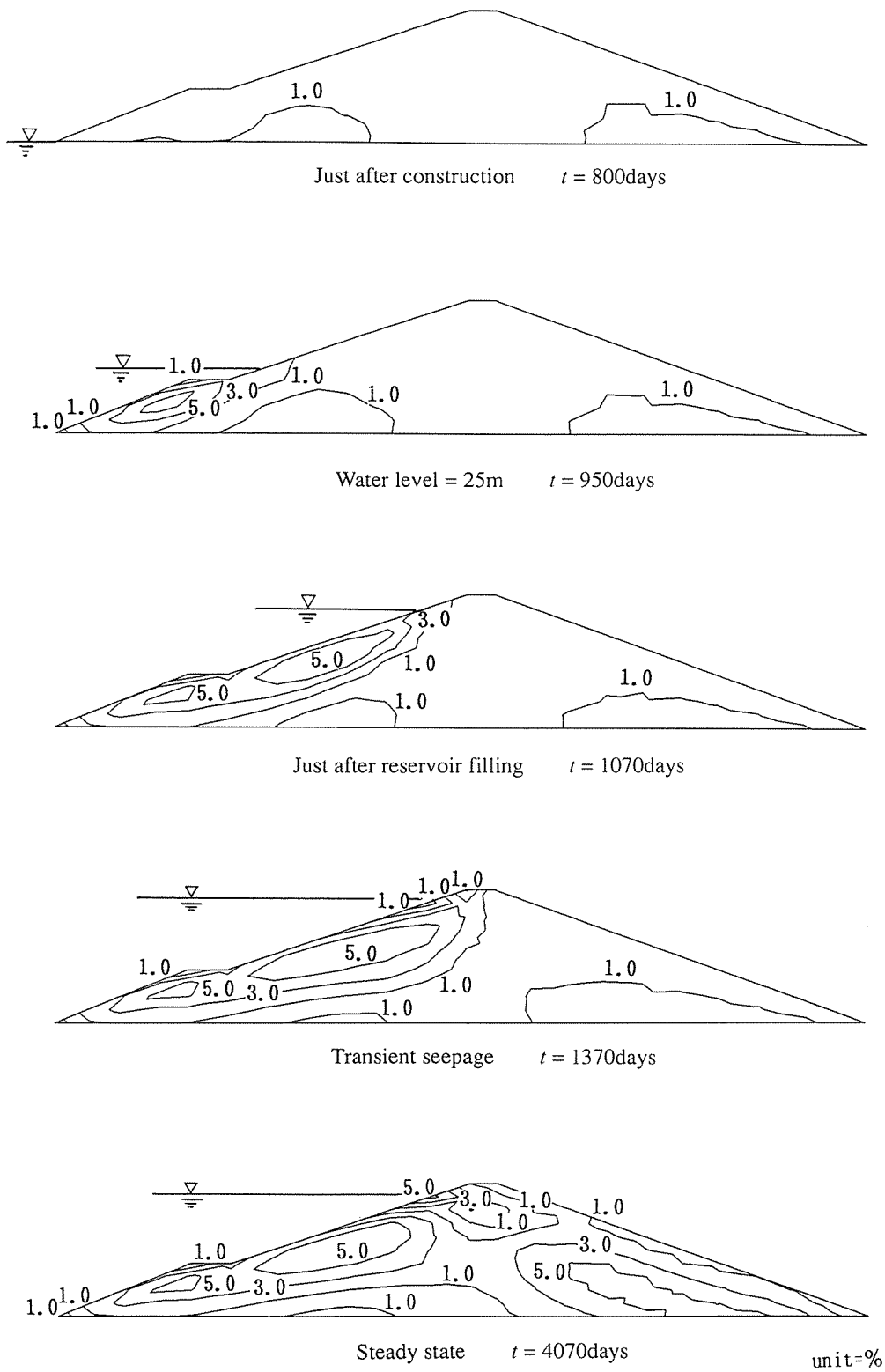


Fig. 21. The analysis results (shear strain distributions) of an earth-fill dam at each stage

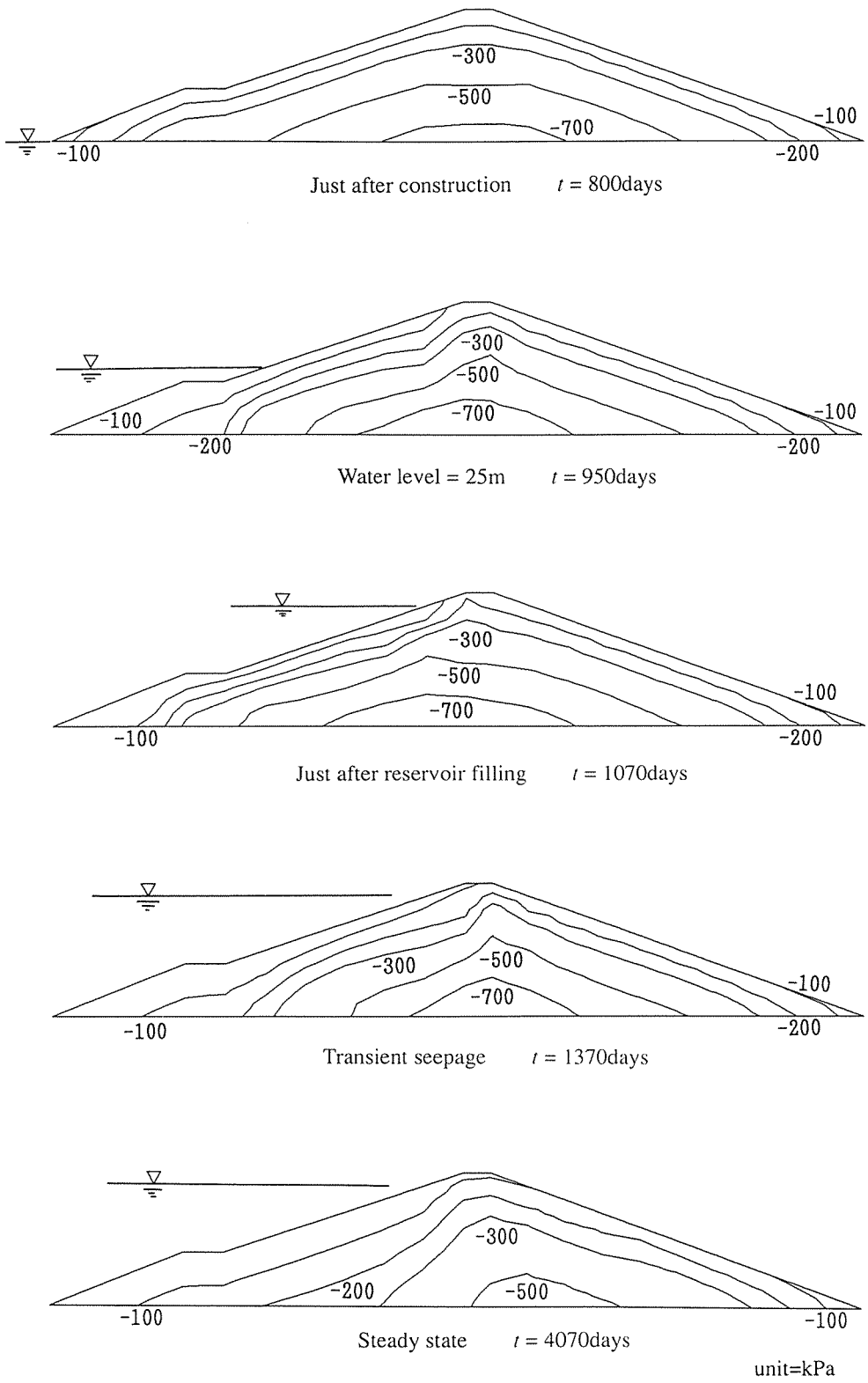


Fig. 22-(a)

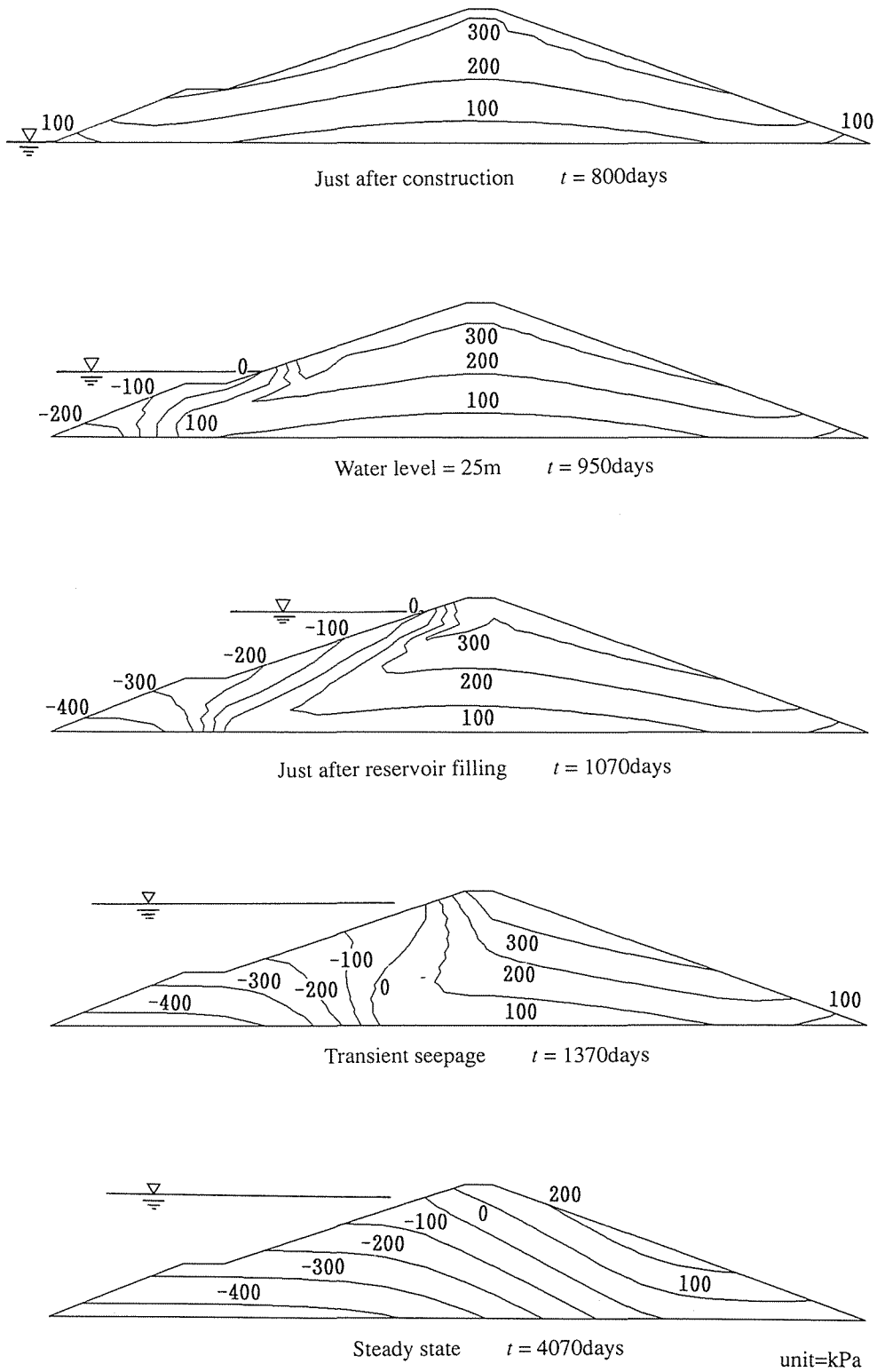


Fig. 22-(b)

Fig. 22. The analysis results (stress distributions) of an earth-fill dam at each stage (a)Vertical stress (b)Pore water pressure

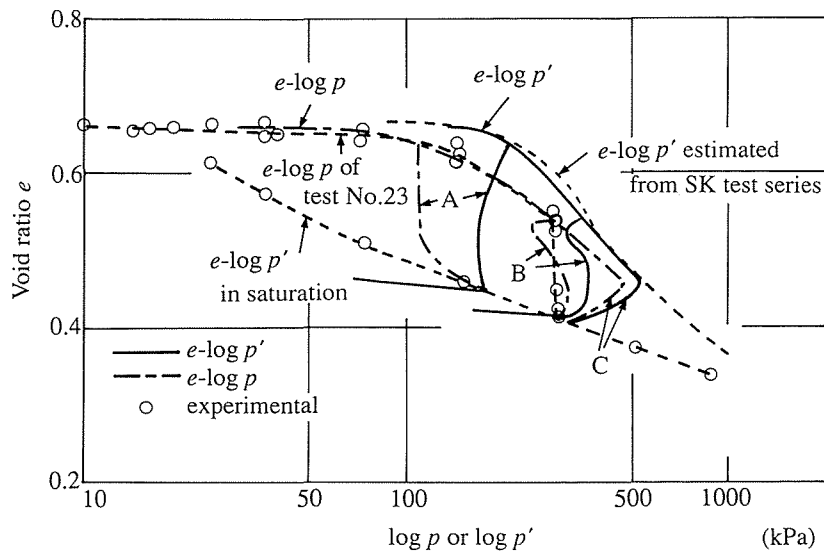


Fig. 23. Relationships between void ratio e and $\log p$ or $\log p'$ at A, B and C points in the dam shown in Fig. 17

represented by introducing the subloading surface model. Such a treatment is useful to analyze many practical problems. The consolidation analysis method employed force equilibrium equations for soil and the Richards' mass conservation equation of pore water as field equations and was formulated by using FEM. The effective stress equations defined in the process of formulating the elastoplastic model were used.

Three simulations concerned with saturation collapse; K_0 consolidation test series, a seepage model test and a virtual earth dam were performed using the consolidation analysis method. The simulation results of K_0 consolidation test series with and without soaking showed that the consolidation analysis method could be applied to the estimation of the saturation collapse behavior measured in the laboratory tests.

The following results of a seepage model test for a compacted unsaturated soil; (1) the values of suction became lower as seepage went on and increased towards the upper corner of the downstream side, (2) the amounts of displacement due to vertical stress were small, (3) the deformation advanced from the upstream side with seepage, could be simulated using the analysis method.

The deformation behavior of an earth-fill dam constructed with a collapsible soil during reservoir

filling was also analyzed by the same method. The behavior of earth-fill dams during reservoir filling is complexly influenced by the application of the water-load, the pore water pressure change in the dam and the collapse due to wetting. Such a complex behavior could not be simulated until the analysis method described above was adopted.

We demonstrated through the simulations that the method was available to analyze geomechanical static problems related to pore water changes, especially saturation collapse behavior.

References

- 1) Alonso, E. E. *et al.* (1990). A constitutive model for partially saturated soils. *Geotechnique* **40**, No. 3:405-430.
- 2) Atkinson, J. H. & Bransby, P. L. (1978). *The mechanics of soils - An introduction to critical state soil mechanics*. McGraw-Hill:18-144.
- 3) Dafalias, Y. F. & Herrmann, L. R. (1982). Bounding surface formulation of soil plasticity, Chapter 10. *In Soil Mechanics - Transient and Cyclic Loads*, edited by G. N. Pande & O. C. Zienkiewicz, John Wiley & Sons, 253-282.
- 4) Dudley, J. H. (1970). Review of collapsing soils. *J. Soil Mech. Foundation Div., Proc. ASCE* Vol. **96**, No. SM 3:925-947.

- 5) Hashiguchi, K. (1980). Constitutive equations of elastoplastic materials with elastic-plastic transition. *J. Appl. Mech. (ASME)* **47**:266-272.
- 6) Hashiguchi, K. (1990). Theory of elasto-plasticity (New version). Asakura - syoten, 1-205 [in Japanese].
- 7) Karube, D. & Kato, S. (1989). Yield function of unsaturated soil. Proc. 12th ICSMFE, Rio de Janeiro, Vol. **1**:615-618.
- 8) Kohgo, Y. (1987). The interpretations and analyses of mechanical behavior of partly saturated soils using elastoplastic models. Proc. Symp. on Unsaturated Soils, Osaka, Japan, JSSMFE, 69-78 [in Japanese].
- 9) Kohgo, Y. (1992). Deformation analysis of fill-type dams during reservoir filling. Proc. 4th Int. Symposium Numer. Models Geomech. NUMOG IV, Swansea, Balkema, Vol. **2**:777-787.
- 10) Kohgo, Y. *et al.* (1991). Elastoplastic constitutive modelling for unsaturated soils. Proc. 7th Int. Conf. Computer Meth. Adv. Geomech., Cairns, Balkema, Vol. **1**:631-636.
- 11) Kohgo, Y. *et al.* (1993). Theoretical aspects of constitutive modelling for unsaturated soils. *Soils and Foundations* Vol. **33**, No. 4:49-63.
- 12) Kohgo, Y. *et al.* (1993). Verification of the generalized elastoplastic model for unsaturated soils. *Soils and Foundations* Vol. **33**, No. 4:64-73.
- 13) Kohgo, Y. (1994). Study on mechanical properties of unsaturated soils and stability of soil structures. Ph. D. Thesis, University of Tokyo, 1-250 [in Japanese].
- 14) Kohgo, Y. *et al.* (1995). Closure - Verification of the generalized elastoplastic model for unsaturated soils. *Soils and Foundations* Vol. **35**, No. 1:173-174.
- 15) Kohgo, Y. & Yamashita, T. (1988). Finite element analysis of fill type dams - Stability during construction by using the effective stress concept. Proc. 6th Int. Conf. Numer. Methods Geomech., Innsbruck, Balkema, 1315-1322.
- 16) Maswoswe, J. (1985). Stress paths for a compacted soil during collapse due to wetting. Ph. D. Thesis, University of London, 1-485.
- 17) Matyas, E. L. & Radhakrishna, H. S. (1968). Volume change characteristics of partially saturated soils. *Geotechnique* **18**, No. 4:432-448.
- 18) Nakagawa, K. *et al.* (1985). Finite element analysis of pore pressure behavior of rockfill dam. Proc. 5th Int. Conf. Numer. Methods Geomech., Nagoya, Balkema, 919-926.
- 19) Nobari, E. S. & Duncan, J. M. (1972). Effect of reservoir filling on stresses and movements in earth and rockfill dams. Report No. TE-72-1, University of California, Berkeley.
- 20) Ortiz, M. & Simo, J. C. (1986). An analysis of a new class of integration algorithms for elastoplastic constitutive relations. *Int. J. Numer. Methods Eng.* **23**:353-366.
- 21) Tanaka, T. (1979). Generalized elasto-plastic model of cohesive soils including strain softening and finite element analyses. *Bull. Nati. Res. Inst. Agric. Eng. Japan* No. **18**:101-122 [in Japanese].
- 22) Zienkiewicz, O. C. & Humpheson, C. (1977). Viscoplasticity : A generalized model for description of soil behaviour. Numer. *In Meth. Geotech. Eng.*, edited by Desai, C. S. and Christian, J. T., New York, McGraw-Hill, 116-147.

飽和コラップス挙動の解析手法について

向後 雄二

国際農林水産業研究センター生産利用部
(〒305 茨城県つくば市大わし1-2)

摘 要

飽和コラップス挙動を予測するために、不飽和土を対象とした弾塑性モデルを用いた圧密解析手法を示した。ここで示した弾塑性モデルは、二つのサクシオン効果を考慮している。二つのサクシオン効果は、(a) サクシオンの増加による有効応力の増加 (b) サクシオンの増加による降伏応力と塑性変形に対する抵抗の増加である。サクシオン効果 (a) は、不飽和土に対する有効応力式を提案し、それによって見積もられた有効応力を用いて応力不変量を評価することによって、弾塑性モデルへ導入された。サクシオン効果 (b) は、サクシオンが増加および減少することによって、降伏面が拡大および縮小するとして、弾塑性モデルの中へ導入された。さらに、このモデルでは、弾性から塑性への移行をスムーズに行うために、下負荷面モデル (Subloading surface model) を採用した。これにより、応力-ひずみ関係は滑らかな曲線となり、より実際的な応力-ひずみ関係を表現できる。このように、このモデルは古典塑性論の枠組みを越え、一般化塑性 (繰返し塑性) 論の枠組みに入るモデルであり、今までに例を見ない斬新なモデルである。さらに、この論文で示した弾塑性モデルへのサクシオン効果の導入方法を用いれば、塑性体積ひずみを硬化パラメータとするモデルであればどのようなモデルでも、不飽和土を対象としたモデルにすることができる。これにより、すでに飽和土の分野で開発された多くの優れたモデルを、不飽和土に適用することができる。

圧密解析法では、飽和土に対するBiotの圧密理論を不飽和土にどのように拡張するかが問題となる。特に、間

隙流体と土骨格の応力分担則 (有効応力則) と不飽和土の応力-ひずみ関係をどのように評価するかが最大問題である。これらの問題は、上述したサクシオン効果の考察により解決した。通常地盤工学の分野で遭遇する多くの問題では、間隙空気圧を考慮する必要がないことより、この論文では、土に対する力の釣り合いと間隙水圧に対する質量保存則を場の方程式とした。有限要素法を用いて定式化し、材料非線形性を考慮するために、Newton-Raphson法による定式化が示された。塑性応力の計算手順として効率的な一般化リターンマッピング法を用いた。この方法により、飽和コラップス挙動を首尾良く計算できる。

この圧密解析法を用いた三つのシミュレーションを示した。一つ目は、要素試験 (K_0 圧密試験) のシミュレーションで、飽和コラップス過程での体積変化および応力径路がうまく再現された。二つ目は、浸透模型実験の解析で、浸透過程でのサクシオンおよび垂直変位 (沈下) の経時変化を定量的にかなりの精度で再現できた。三つ目は、コラップス土 (飽和コラップスを引き起こす土) で造られた仮想の均一型アースダムの築堤およびそれに続く貯水時の解析例で、解析結果は、今まで実際のダムで観測された貯水時の複雑なダム挙動をうまく説明できるものであった。

このように、ここで示した圧密解析手法は、飽和コラップスを含めた間隙水圧の変化に関連した地盤工学分野の静的な問題に適用可能である。

キーワード：有効応力、圧密解析、土の構成式、塑性、不飽和土